



Baldwin Nsonga  · Jordi Ventosa-Molina · Denis Koschichow · Jochen Fröhlich · Stefan Gumhold · Gerik Scheuermann

Visual analysis of the impact of periodic wakes on the pressure side of a turbine blade

Received: 24 January 2023 / Revised: 9 March 2023 / Accepted: 4 April 2023
© The Author(s) 2023

Abstract Turbines are core components in jet engines for flight propulsion, power plants, and other important energy conversion processes. They are composed of successive rows of blades so that wakes of upstream blades reach subsequent blades where they perturb the flow in an unsteady manner. At the point where a wake reaches the downstream blades, the perturbation forms a so-called negative jet. In this work, we show that the negative jet partially fulfills the conditions of an anti-splat. Based on this finding, we enhance an anti-splat detection algorithm developed by the present authors in previous work and apply it to direct numerical simulation data of a turbine cascade with unsteady wakes. This provides a sound framework and suitable visualization approaches to investigate the phenomenon even in very complex conditions, as is the alteration of the boundary layer flow along the pressure side of a turbine blade. The approach allows a very clear visualization of this interaction, which was not possible to evidence with previous methods, providing new insight into the physics of this flow. The use of flow paths shows up to which point wakes affect the boundary layer along the blade. The reported physical analysis, made possible by the proposed approach, demonstrates the usefulness of the method for the application domain. The generalization to flows in compressors, pumps, and blade-tower interaction in wind engineering and other fields is possible.

Keywords Flow visualization · Turbine cascade · Periodic wakes · Wake boundary interaction

1 Introduction

In gas turbines, compression and expansion are typically performed through several stages, each consisting of a stator-rotor pair, where the latter rotates. Between each row of blades, the flow exiting a row becomes

B. Nsonga (✉) · G. Scheuermann
Institute of Computer Science, Leipzig University, 04109 Leipzig, Germany
E-mail: nsonga@informatik.uni-leipzig.de

G. Scheuermann
E-mail: scheuermann@informatik.uni-leipzig.de

D. Koschichow · J. Fröhlich
Institute of Fluid Mechanics, TU Dresden, 01062 Dresden, Germany
E-mail: jochen.froehlich@tu-dresden.de

J. Ventosa-Molina
Heat Engines Department, Universitat Politècnica de Catalunya, 08222 Terrassa, Spain
E-mail: jordi.ventosa-molina@upc.edu

S. Gumhold
Institute of Software and Multimedia Technology, TU Dresden, 01187 Dresden, Germany
E-mail: stefan.gumhold@tu-dresden.de

the inflow of the next row. A sketch of a turbine stage is depicted in Fig. 1. Along each blade, a boundary layer develops, resulting in a velocity deficit behind the blade, denoted as *wake*. The wakes of the upstream row then affect the blades of the downstream row. As the wake does not span the whole blade pitch (cf. Fig. 2), it causes an uneven distribution of the inflow conditions to the downstream stage. Furthermore, this interaction between rows is not static. The relative motion between the blades implies a low-frequency unsteady effect of the upstream blades on the downstream ones perturbing the flow structure periodically (Hodson and Howell 2005; Wu and Durbin 2001).

The interaction between incoming wakes and the blade boundary layer is a critical aspect. Turbines extract energy from the flow by deflecting and expanding it through blade rows. The flow characteristics around the blade, namely the boundary layer and its state, determine the forces acting on it to a large extent and, consequently, the energy that can be extracted from a turbine stage and the energy loss. Due to the different nature of the flow in laminar and turbulent boundary layers, correctly characterizing where transition from laminar to turbulent takes place and by which mechanism is critical for the design process (Mayle 1991; Walker 1993).

The present case study addresses the effect of incoming wakes on the boundary layer of the downstream blade in the context of anti-splats. Perot and Moin (1995a, 1995b) defined a splat as a region where fluid approaches a boundary, which may be a solid wall or a free surface, and spreads outward. Accordingly, an anti-splat is a region where tangentially moving fluid converges and detaches from the wall into the bulk flow. We study the effect of incoming wakes by means of a recently developed (anti-)splat visualization technique (Nsonga et al. 2020, 2020). In contrast to our previous work, it is not used for turbulent fluctuations but applied to a moving periodic (anti-)splat feature drowned in a mean flow with additional turbulent fluctuations.

The present work focuses on the wake-boundary layer interaction with the following goals:

- (I) From a physical analysis perspective, the aim is to characterize the volumetric interaction of wake and boundary layer by evidencing the magnitude and position of the perturbation caused by the wake on the boundary layer.
- (II) Modification of the existing anti-splat detection technique to detect a wake impact on a turbomachinery blade.
- (III) Development of an intuitive, surface-based visualization scheme representing the volumetric wake-boundary layer interaction, enabling a direct analysis.

2 Case

2.1 Configuration

The flow in a linear turbine cascade equipped with *T106A* profiles is a widespread test case in the turbomachinery community (Weiss and Fottner 1995; Engber and Fottner 1996; Duden et al. 1999; Cardamone et al. 2002; Wu and Durbin 2001; Wissink 2003; Michelassi et al. 2003; Stieger and Hodson 2003; Ciorciari et al. 2014; Michelassi et al. 2015). The experimental cascade considered is composed of 7 blades, each with a chord of $c = 100$ mm separated by a pitch of $p = 79.9$ mm. Blades are placed with a stagger angle of 59.28° and the angle of attack of the flow, i.e., its angle with respect to the x -axis, is $\alpha = 37.7^\circ$. With this configuration, the axial chord length is $L_{ref} = c_{ax} = 85.88$ mm.

The physical domain simulated corresponds to a subset of the experimental domain, where only the passage between two blades is simulated, as depicted in Fig. 2, with periodic boundary conditions in the y -direction, a standard approach in the community. The domain has an extension of $L_z = 85$ mm in spanwise direction and features a sidewall at $z = 0$.

All extensions in space—and, hence, all coordinates—are made non-dimensional using the axial chord length c_{ax} . The reference flow speed for the simulation is $U_{ref} = U_{in} = 80$ m/s. The Reynolds number based on the above quantities is $Re = 5 \cdot 10^4$. In the simulation described below, the density ρ of the flow was set constant.

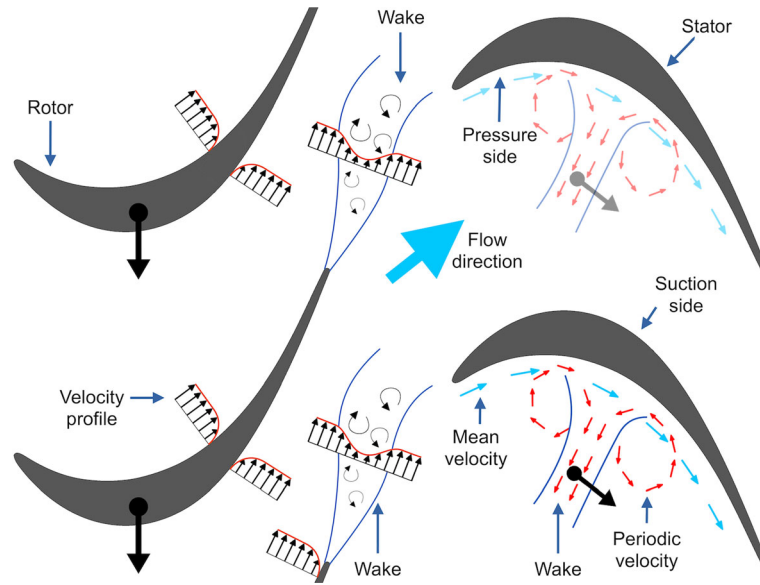


Fig. 1 Illustration of a rotor-stator interaction in a turbine cascade. Wakes of the upstream rotor interact with the downstream stator, producing the so-called negative jet structure, based on Hodson and Dawes (1998). Blue vectors indicate the mean flow $\bar{\mathbf{u}}(\mathbf{x})$ and red vectors indicate the periodic flow contribution $\bar{\mathbf{u}}(\mathbf{x}, \phi)$ (cf. Eq. 1). The decomposition of the flow field illustrated here is detailed later in Sect. 5

2.2 Dataset

The data employed here were generated in Koschichow et al. (2014) using a very fine grid resolving all turbulent eddies, thus qualifying as a direct numerical simulation (DNS). Specifically, an entirely structured curvilinear hexagonal grid was used with local grid stretching, as shown in Fig. 2. The grid consists of 1154, 290, and 548 cells in the x -, y - and z -direction, respectively. Grid stretching was also employed toward the sidewall. Parallelization was accomplished by domain decomposition using 448 blocks, which were merged into a single block for post-processing.

Simulations were carried out using the in-house code LESOCC2 (Large Eddy Simulation on Curvilinear Coordinates version 2). For the sake of brevity, we refer to (Wang et al. 2007; Wissink and Rodi 2008; Hinterberger et al. 2008) for details of the code and validation.

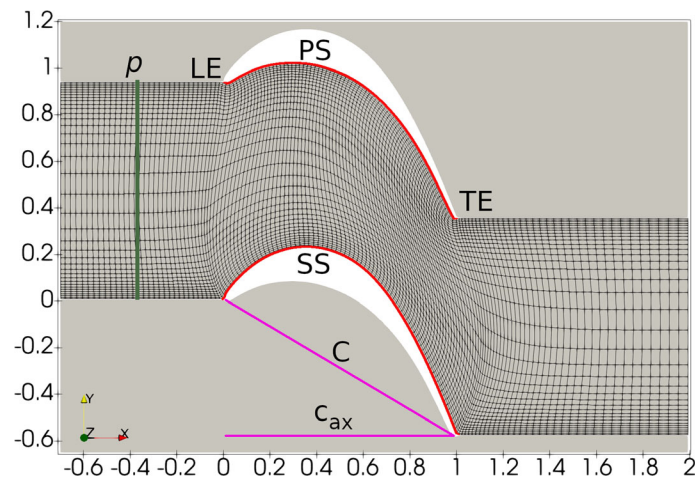


Fig. 2 Two-dimensional cut through the physical domain, $z = \text{const}$. Only one passage between two blades is simulated, highlighted by the computational grid (only 1 of 8 lines is shown). Different geometrical quantities are also marked: pressure (PS) and suction (SS) side in red, blade chord c , its axial projection c_{ax} in rose, and blade pitch p in green. The leading edge (LE) and trailing edge (TE) are also marked. Image adapted from Nsonga et al. (2020)

The same case without wakes was studied previously by means of a (anti-)splat detector by the authors (Nsonga et al. 2020), focusing on turbulent fluctuations near the wall. In the current work, the new feature is the presence of regular periodic wakes which, in terms of analysis, yields a fundamental difference, as the blade perturbation has a deterministic and a stochastic component. The influence of the wake on the blade row performance, i.e., total pressure losses, was performed in the referenced previous study (Koschichow et al. 2014). Briefly, for the current case, the study found a minor influence on the total pressure losses and a more marked influence on the exit flow angle.

Here, the inlet velocity is the result of superposing the unsteady velocity of a turbulent boundary with instantaneous turbulent velocity data representing the wake of a circular cylinder. The unsteady data for the turbulent boundary layer velocity were generated by a so-called precursor simulation imposing a boundary layer thickness of $\delta = 0.245c_{ax}$. The unsteady wake data were obtained by DNS of the flow around a cylinder (Wissink and Rodi 2008) and provided by these authors. The wakes were introduced at a position moving with a velocity of $U_{bar,y} = 0.25 U_{ref}$ in pitchwise direction (y-direction). Typically, in turbines the bar pitch p_{bar} would be equal to the blade pitch p (Wu and Durbin 2001). Yet, in Koschichow et al. (2014) the pitchwise separation between the wakes was halved, resulting in $p_{bar} = 0.5p$. The aim of this adjustment was to reduce the simulation time needed to collect enough statistical data and to enhance the impact of the wakes, which was the research question in that study. The resulting period of the periodic disturbances is $T = (p_{bar}/c_{ax})/(U_{bar,y}/U_{ref}) = 1.861$. The simulation of 36 periods required about six weeks on a high-performance system with 448 cores (Intel E5-2690 (Sandy Bridge)). The data generated and used for the present work covers entire flow fields over $N_T = 36$ periods, excluding the start-up phase, stored at a time interval of $\Delta t_s = 4.65 \cdot 10^{-2} c_{ax}/U_{ref}$, yielding 40 fields per period. Each flow field was stored on the entire computational grid. The total amount of data was 6.9TB. Further detail on the remaining boundary conditions can be found in Nsonga et al. (2020), Koschichow et al. (2014).

3 Application background

3.1 Periodic wakes

The interaction between blade rows is sketched in Fig. 1. The wake is the result of flow navigating around an upstream blade. In general, a wake is a region of low momentum behind a bluff body, e.g., a sphere, a cylinder, aerodynamic profile and is a result of viscous and pressure effects on such bodies. In a wake, the velocity in the center region is smaller than in the outer flow, while velocity fluctuations are higher. As the flow progresses away from the bluff body, the width of the wake grows. At the same time, the intensity of the fluctuations decreases.

As mentioned in the introduction, the interaction between rotor and stator is unsteady. Due to the relative motion between blades, wakes sweep the downstream blade from leading edge (LE) to trailing edge (TE). The effect of migrating wakes has been extensively studied (Hodson and Dawes 1998; Wu and Durbin 2001; Wissink 2003; Michelassi et al. 2003; Stieger et al. 2003; Hodson and Howell 2005; Sarkar 2008; Busse et al. 2014; Ciorciari et al. 2014; Koschichow et al. 2014; Wissink et al. 2014; Davide et al. 2017). The main effects involve changes in the transition to turbulence and flow separation (Mailach and Vogeler 2004; Berrino et al. 2015). Additionally, Wu and Durbin (2001) argued that due to this interaction, the vortical structures in the stage are a response rather than a result of instabilities in the boundary layer. Zaki (2013) showed that the boundary layer acts as a sort of low pass filter, filtering out the high frequency perturbations and responding mostly to low frequency perturbations. This makes it sensitive to the large-scale feature of the negative jet requiring an appropriate characterization of the interaction.

Due to the configuration of turbine stages and the specific relative motion, as depicted in Fig. 1, a *negative jet* occurs at the pressure side of the downstream blade (cf. Fig. 3). In terms of the coordinate system of the wake, the wall annihilates the axial velocity, so that inflow into the wake from the side is generated, as visualized in the right part of the figure. Another viewpoint is to interpret the interaction of the wake with the wall as a kind of inverse jet suctioning flow from a surface, hence motivating the term “negative jet” (Hodson and Dawes 1998; Hodson and Howell 2005). In a jet configuration, the center of the jet has the highest velocity and at the impact location, the flow spreads away from the center. In the *negative jet* configuration, the current one, the flow direction is inverted. The jet’s center features a lower velocity, and the flow is oriented toward the center from the sides. The situation is different at the suction side where the wakes deform and gradually approach the wall, usually with an impact on the near-wall turbulence (Wu

and Durbin 2001; Michelassi et al. 2003; Koschichow et al. 2014). This is fundamentally different and not addressed here.

3.2 Boundary layers

Sufficiently high-Reynolds-number flow fields in the vicinity of surfaces can be conceptually split into two regions of different sizes: near surfaces viscosity effects are significant and must be accounted for, and away from surfaces these effects do not have such a prevalent role (Schlichting and Gersten 2017). The former region is termed a boundary layer and is of particular importance because it determines the aerodynamic resistance. One component of it is the friction, which depends on the velocity gradient and the fluid viscosity. Furthermore, heat transfer is also dependent on the boundary layer state.

Typically, in flows around aerodynamic bodies the boundary layer starts as laminar, where velocity fluctuations are very low, and becomes turbulent further downstream, after a so-called transition. This dual behavior is reflected by the friction at the surface. In the laminar region it decreases until the transition point, where it increases within a short distance and thereafter starts to decrease again, but at a lower rate.

The performance of turbine blades is highly dependent on the boundary layer along blades (Denton 1993; Wheeler et al. 2017), in particular viscous shear and turbulence production (Spencer et al. 2021). Furthermore, depending on the state of the boundary layer, flow separation, i.e., stall, may arise leading to high performance losses (Mailach and Vogeler 2004; Hodson and Howell 2005; Mayle 1991). Due to the nature of the wakes, they represent a periodic high intensity and localized perturbation of the boundary layer. These perturbations can trigger instabilities of the flow. Hence, it is critical to understand their effect on the boundary layer. Additionally, the wakes carry a certain level of turbulence which also affects the boundary layer (Zaki et al. 2010; Schreiber et al. 2000; Muthanna 2002; Scillitoe et al. 2007). With regard to the turbulent component of the wakes, Zaki (2013) showed that the boundary layer acts as a sort of low pass filter, filtering out the high frequency perturbations and responding mostly to low frequency perturbations. In the present analysis, the focus is on the periodic contribution, later defined in Sect. 5.

4 Related work

4.1 Instantaneous and steady flows

Flow properties are commonly depicted through the visualization of 2D cuts of the flow domain. (cf. Fig. 3). These properties can range from direct simulation results (e.g., pressure, temperature, velocity components, velocity magnitudes) to statistics and decomposition results (e.g., velocity fluctuation, mean flow).

Common techniques in flow visualization are topological methods which reveal the topological skeleton. This skeleton consists of critical points and separatrices which segment the flow domain into regions of similar flow behavior. Particles seeded within such a segment share the same origin and destination (Helman and Hesselink 1989, 1991). Vector field topology, in general, is only applicable for steady flows. Laramee et al. (2007) presented an overview of various studies concerned with this topic. These techniques help to advance the general understanding of flows. However, we are aware that the present case is already well-understood, and similar configurations have been extensively studied (cf. Sect. 3). Regarding the stated research question, it is evident that techniques concerned with surface-level flow patterns are of interest. A common method is the visualization of detachment and attachment lines (Chapman and Yates 1991). To better understand the volumetric interaction between wake and boundary layer, analyzing detachment lines is not sufficient.

4.2 Unsteady flows

Various studies are concerned with the application of vector field topology for time-dependent flows (Bujack et al. 2020). Nevertheless, most commonly used unsteady analogy to vector field topology in unsteady flows is so called Lagrangian coherent structures (LCS). They indicate manifolds at which flows separate or converge, separating regions of different time-dependent flow behavior. Various techniques for the computations of LCS based on the Finite-Time-Lyapunov Exponent (FTLE) were proposed and discussed by Haller and Yuan (2000), Haller (2015). Comparable to vector field topology, LCS are too generic for the present case, as they do not allow a purposive investigation of our research question. In addition,

fluctuations result in a high amount of clutter and with no inherent hierarchy of visible ridges investigating the wake impact on the boundary layer is challenging. Unsteady techniques are also applicable at surface level, e.g., surface FTLE (Garth et al. 2008), or (anti-)splat detection (Nsonga et al. 2020). Analogous to their steady counterparts, they are not sufficient to analyze the volumetric interaction between the boundary layer and periodic wakes.

The concept of periodic wakes (cf. Fig. 1) as a flow feature suggests that its characteristics depend on the chosen frame of reference. Wiebel et al. (2005, 2007) introduced localized flow analysis. In their approach, they subtract the boundary-induced potential flow from the original flow for further analysis. A body of publications in flow visualization concerned with objectivity applies reference frame changes for time-dependent flow fields to extract meaningful flow features, see, for instance, Bhatia et al. (2014); Günther et al. (2017); Hadwiger et al. (2019); Rojo and Günther (2020). Even though these methods are helpful, it would require an extensive discussion on how to interpret the resulting flow fields in the new reference frame physically. We can safely circumvent these discussions, as fluid dynamics literature provides a useful and well-established tool for flows under periodic perturbations. Given a perturbation with a known frequency, or period, a turbulent flow field can be decomposed into three distinct components by a triple decomposition into a time invariant mean, a fluctuating component associated with the known frequency, and a turbulent component (Hussain and Reynolds 1970). More details on the triple decomposition are given later in the following section.

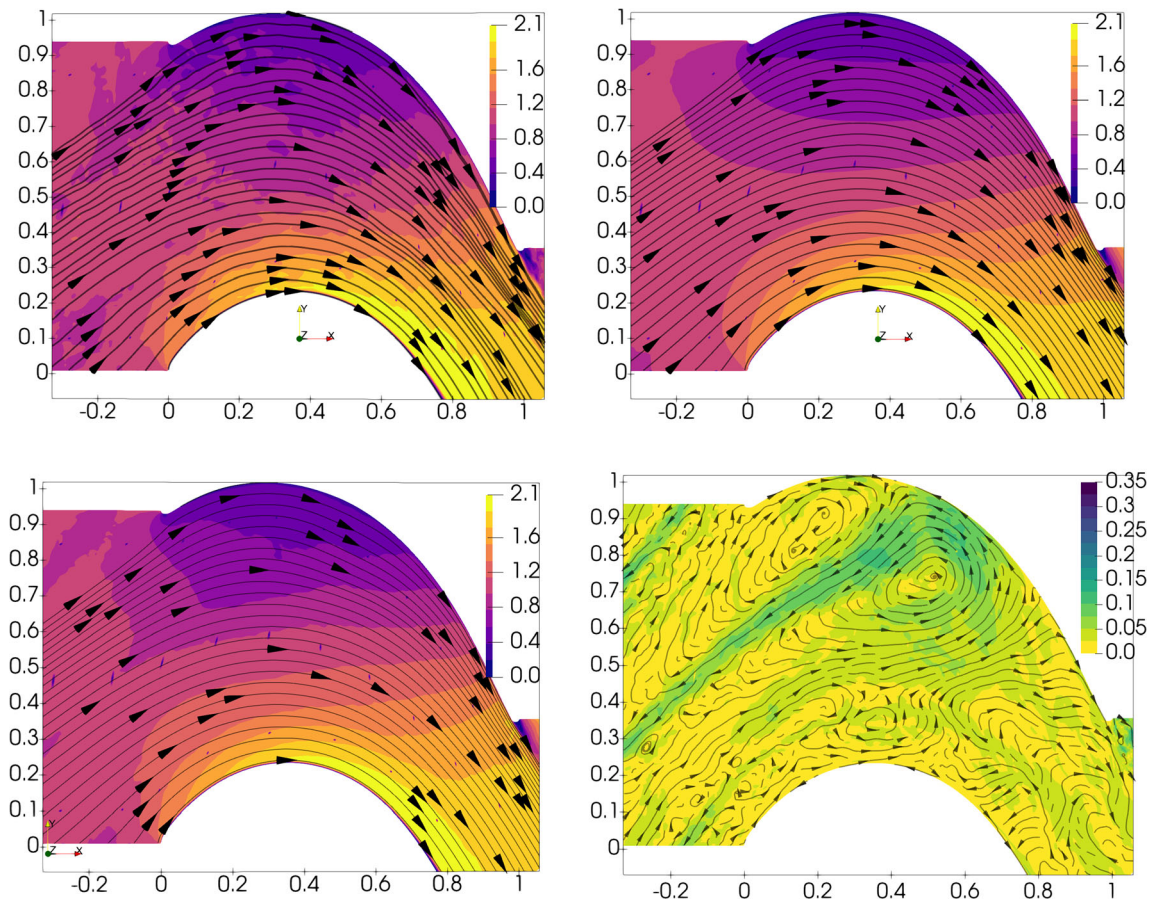


Fig. 3 Visualization of the different components of the velocity field by two-dimensional streamlines in the plane $z/c_{ax} = 0.5$. Arrows denote flow direction, but not magnitude. Color palette denotes magnitude of the respective velocity vector. (Top left) instantaneous field $\mathbf{u}(\mathbf{x}, t)$ (for the last computed time $t = 68.64 \phi = 35/40$); (top right) time averaged field $\bar{\mathbf{u}}(\mathbf{x})$; (bottom left) phase averaged field $\tilde{\mathbf{u}}(\mathbf{x}, \phi)$ for $\phi = 15/40$; (bottom right) phase perturbation field $\tilde{\tilde{\mathbf{u}}}(\mathbf{x}, \phi)$ for $\phi = 15/40$

5 Triple decomposition

5.1 Definition

Consider a velocity field $\mathbf{u}(\mathbf{x}, t)$ where \mathbf{x} is a point in the computational domain $\Omega \subset \mathbb{R}^3$ and t time. The classic Reynolds decomposition, commonly used for the analysis of turbulent flows, characterizes the instantaneous flow $\mathbf{u}(\mathbf{x}, t)$ as the sum of a time-averaged contribution $\bar{\mathbf{u}}(\mathbf{x})$ and a fluctuation around it $\mathbf{u}'(\mathbf{x}, t)$.

For flows with periodic features, the fluctuation $\mathbf{u}'(\mathbf{x}, t)$ can be decomposed into a regular periodic contribution $\tilde{\mathbf{u}}(\mathbf{x}, \phi(t))$ and an irregular turbulent contribution $\mathbf{u}''(\mathbf{x}, t)$, where $\phi(t) = \text{mod} \{t - t_0, T\}/T$ is the phase angle, T the period, and t_0 a point in time defining the instants when $\phi = 0$. This results in the triple decomposition (Hussain and Reynolds 1970)

$$\mathbf{u}(\mathbf{x}, t) = \bar{\mathbf{u}}(\mathbf{x}) + \tilde{\mathbf{u}}(\mathbf{x}, \phi(t)) + \mathbf{u}''(\mathbf{x}, t). \quad (1)$$

5.2 Computation of triple decomposition

To obtain $\tilde{\mathbf{u}}$ for each phase angle $\phi \in [0; 1)$, averaging is performed over all instants corresponding to the same phase angle, i.e.,

$$\hat{\mathbf{u}}(\mathbf{x}, \phi) = \frac{1}{N_T} \sum_{n=1}^{N_T} \mathbf{u}(\mathbf{x}, t_0 + \phi T + nT), \quad (2)$$

where N_T is the number of periods available in the data. This number should be sufficiently large to obtain a good approximation of the limit $N_T \rightarrow \infty$. The periodic contribution then is

$$\tilde{\mathbf{u}}(\mathbf{x}, \phi) = \hat{\mathbf{u}}(\mathbf{x}, \phi) - \bar{\mathbf{u}}(\mathbf{x}). \quad (3)$$

For the practical computation of $\tilde{\mathbf{u}}$, ϕ is discretized by decomposing the interval $[0; 1)$ into N sub-intervals, or bins, $[(i-1)/N; i/N)$, $i = 1, \dots, N$. The bin is addressed by the phase $\phi = i/N$ with $i = 1, \dots, N$ in the following, or directly by its number i . Usually, averaging over all phases within such a bin is applied, but in the present case only one data set per period falls into this bin. For the current analysis $N = 40$.

Figure 3 depicts all non-turbulent contributions defined above in a plane $z = \text{const.}$ using a particular phase as an example. As depicted in Fig. 1, at the point where the wake reaches the blade on the pressure side, the flow structure is akin to a “negative jet”. It is obvious that this negative jet is not directly observed in the mean flow field. It rather is a feature of the phase fluctuation $\tilde{\mathbf{u}}(\mathbf{x}, \phi)$, where it is seen very clearly (cf. Fig. 3, bottom right). Although the wake is qualitatively visible in the 2D slice, an unambiguous extraction of the 3D region wake region for a quantitative analysis is not straightforward. The most significant issue is that most extraction approaches would require thresholds, which are hard to derive in a physically meaningful way for an arbitrary flow.

Through this decomposition periodic perturbations are decomposed into several phases, enabling the independent analysis of the flow field for each phase.

5.3 Perturbation

To characterize the level of perturbation induced by the passing wakes, the perturbation is defined here based on the periodic perturbation and the mean velocity

$$d(\mathbf{x}, \phi) = \frac{\|\tilde{\mathbf{u}}(\mathbf{x}, \phi)\|}{\|\bar{\mathbf{u}}(\mathbf{x})\|}. \quad (4)$$

This ratio evidences clearly the strength by which the wake perturbs the mean flow in a particular phase.

6 Boundary layer penetration

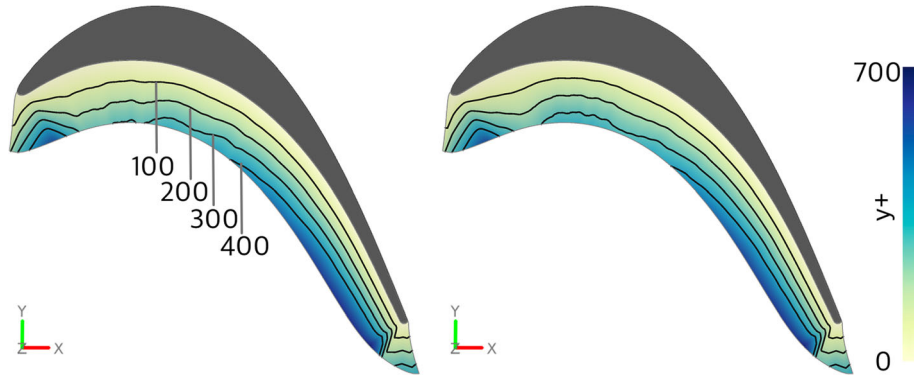


Fig. 4 Visualization of the computed dimensionless distance y^+ in the plane $z/c_{ax} = 0.5$ for the first 96 slices at the pressure side. y^+ for phase $\phi = 5/40$ (left) and phase $\phi = 15/40$ (right) is displayed using color mapping and contour lines

6.1 Non-dimensional wall distance

A common way to characterize the flow near surfaces is through a non-dimensional wall distance, typically denoted as y^+ (here not to be confused with the y -direction in Fig. 2) and defined as

$$y^+ = \frac{y_n}{l_\tau} = \frac{u_\tau y_n}{\nu}, \quad (5)$$

where y_n denotes the distance to wall, l_τ the (local) viscous length scale and $u_\tau = \sqrt{\tau_w/\rho}$ the friction velocity with the local wall shear stress τ_w at the wall and the fluid density ρ . The wall shear stress is computed from the normal gradient of the tangential velocity and the dynamic viscosity $\mu = \rho\nu$.

Based on this distance, the boundary layer (BL) can be characterized with small values of y^+ indicative of regions close to a wall where viscosity effects dominate. A rich theory is available where the physical properties of a turbulent boundary layer flow are discussed as a function of y^+ and the BL decomposed into different zones (Schlichting and Gersten 2017; Pope 2000). For the present case it is to be stressed that the boundary layer along the pressure side is far from the canonical case of a boundary layer along a flat plate with constant pressure. Effects such as transition, streamline curvature and pressure gradient introduce marked deviations with respect to the canonical case (Michelassi et al. 2003, 2015). Nevertheless, we still apply y^+ in this analysis as it contains valuable information for the domain scientists.

6.2 Computation of the non-dimensional distance

In the present work, the dimensionless wall distance field is a scalar field close to the wall, $y^+(\mathbf{x}, \phi)$, computed in a near-wall subset of the domain presented in Sect. 2.2. Here, we construct a near-wall domain by first computing the wall normals at the pressure side of the blade. In the following, we denote the surface at the pressure side of the turbine blade as $B \subset \partial D$, where D is the domain. We then construct a curvilinear grid G_B by using the normal and the surface tangent vectors.

The dimensionless wall distance is commonly computed with the mean flow $\bar{\mathbf{u}}(\mathbf{x})$. Here, we account for the effect of the regular, periodic changes of the flow field by using the phase averaged flow field $\mathbf{u}(\mathbf{x}, \phi)$ (Eq. 2).

We can now compute the phase averaged wall shear stress for every surface-level grid point $\mathbf{x}_w \in G_B \cap B$ as $\hat{\tau}_w(\mathbf{x}_w, \phi) = \rho\nu \|\nabla \hat{\mathbf{u}}(\mathbf{x}_w, \phi) \cdot \mathbf{n}(\mathbf{x}_w)\|$, where $\nabla \hat{\mathbf{u}}(\mathbf{x}_w, \phi)$ is the spatial gradient and $\mathbf{n}(\mathbf{x}_w)$ is the wall-normal. With the resulting $\hat{\tau}_w(\mathbf{x}_w, \phi)$, we can compute the dimensionless distance with Eq. 5 at every point $\mathbf{x} \in G_B$, where y_n is the minimal distance between \mathbf{x} and the surface B . This results in a 3D scalar field $y^+(\mathbf{x}, \phi)$ (cf. Fig. 4). After extracting a volume approximation of the wake impact, we will utilize this scalar field to quantify the boundary-layer penetration, as discussed in Sect. 9.

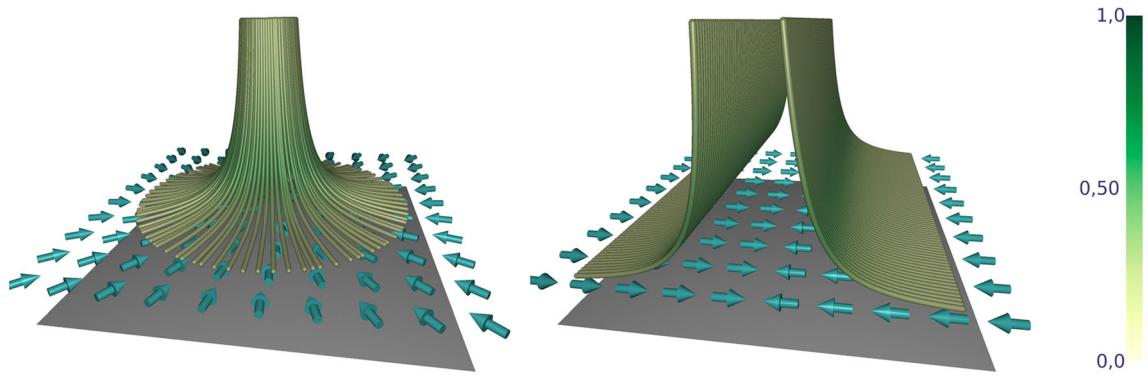


Fig. 5 Ideal anti-splat flow pattern (*left*) and ideal impinging wake (*right*). Displayed are streamlines with the coloring according to the velocity magnitude

7 From anti-splat to wake impact

7.1 Anti-splat at the pressure side

The flow pattern of the periodic contribution $\tilde{\mathbf{u}}(\mathbf{x}, \phi)$ in Fig. 3 close to the pressure side of the blade is similar to an anti-splat, which Perot and Moin (1995a, 1995b) characterized as a region where tangentially moving fluid converges and detaches from the wall into the bulk flow. It is evident that (anti-)splat detection, presented in our previous work (Nsonga et al. 2020), is useful in detecting the flow region of interest. Here, our goal is not the detection of the wake *per se* but the wake impact on the blade in $\tilde{\mathbf{u}}(\mathbf{x}, \phi)$. Note that a wake can exist, and generally exists, without a downstream obstacle, as visible in the center of Fig. 1 through the two wakes depicted with their velocity deficit. In the present study, we consider the case where the wake is obstructed by a wall at a 90° or a smaller angle with respect to its axis. This is an “impinging wake”, but for simplicity we will occasionally just use the term “wake” to distinguish from a splat.

7.2 Anti-splat definition

In our previous work, we introduced a formal definition for anti-splats near a flat surface $B \subset \partial D$ as regions $S_R \subset D \times T$, where $D \subset \mathbb{R}^3$ is the spatial domain of the flow field and $T \subset \mathbb{R}$ is the time domain, fulfilling certain properties. Employing an offset surface $B^\epsilon := \mathbf{x} + \epsilon \mathbf{n}(\mathbf{x})$, where $\mathbf{x} \in B$, $\mathbf{n}(\mathbf{x}) \in \mathbb{R}^3$ is the boundary normal, and $\epsilon \in \mathbb{R}$ is a small positive value, anti-splats are then defined as follows:

1. Non-empty region $S_R \cap (B^\epsilon \times T) \neq \emptyset$ is simply connected
2. $\forall (\mathbf{x}_0, t_0) \in S_R$: a fluid parcel moving backwards in time toward B along trajectory $s_{\mathbf{x}_0, t_0} : T \rightarrow S_R$ is stretched in the tangential plane parallel to B and compressed in normal direction
3. There exists a closed curve in $S_R \cap (B^\epsilon \times T)$ with a radially inward oriented flow pattern.

An ideal anti-splat is illustrated in Fig. 5, left.

7.3 Modifications to anti-splat definition

The visualization in Fig. 3, the concept of a periodic wake (cf. Fig. 1), and the phase-averaging of the flow lead to the assumption that wakes can be understood as two-dimensional structures. Specifically, it can be assumed that the flow characteristics are constant in the z -direction of the domain. We illustrate the associated ideal wake impact in Fig. 5, right. An ideal anti-splat has rotational symmetry (cf. Fig. 5, left), allowing Condition 2 and 3 to be fulfilled. In contrast, the ideal wake impact has translational symmetry, making it inconsistent with Condition 2 and 3 of the anti-splat definition. This issue necessitates modifications to the anti-splat definition to include the wake impact.

Condition 2 states that a fluid particle moving toward the boundary surface is stretched in the tangential plane. In our previous work, we tested this condition by utilizing the right Cauchy–Green deformation tensor, computed along the trajectory of the fluid volume. We projected the deformation tensor to the

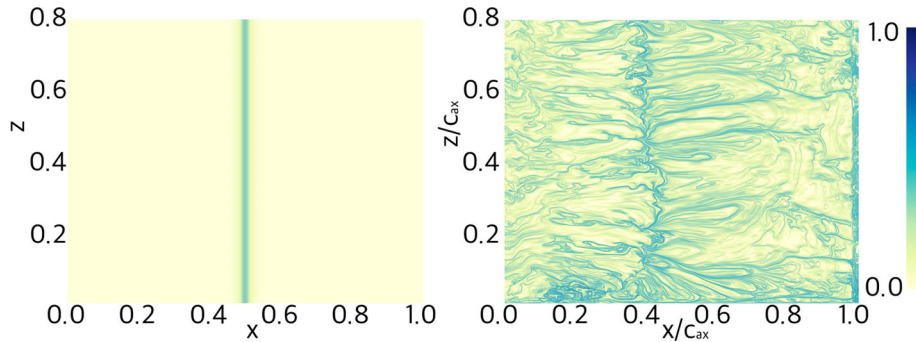


Fig. 6 Surface FTLE (Garth et al. 2008) computed on an artificial ideal wake dataset (cf. Figure 5) (*left*) and in the periodic contribution of the current case $\bar{\mathbf{u}}(\mathbf{x}, \phi)$ in phase $\phi = 15/40$ at a distance of 4 control volumes away from the pressure side (*right*). We used an integration time $\tau = 10$ backward in time

surface, resulting in a 2×2 matrix, and assessed the eigenvalues λ_1, λ_2 . The condition is fulfilled if, $1 < \lambda_1 \leq \lambda_2$. This is caused by the outward acceleration of the fluid volume while being stretched due to the radial flow pattern in the tangential plane (cf. Fig. 5). In contrast, fluid volumes within the ideal wake impact are not subject to radial stretching but to acceleration in the tangential plane. This suggests the following eigenvalue configuration: $1 \approx \lambda_1 < \lambda_2$. This configuration results in a rigorous condition.

In order to validate the usefulness of this modification for the present case, we apply surface FTLE (Garth et al. 2008) to the boundary surface.

Although this method does not help to detect and analyze the wake impact, we can utilize it to qualitatively validate if the periodic wake in the dataset can be regarded as ideal. In the case of an ideal (two-dimensional) wake, we expect a straight and continuous ridge where a separation line would be expected. Figure 6 does not confirm these expectations. Additionally, the surface FTLE visualization reveals structures. The experts attribute this non-smoothness in the z -direction to two issues. (i) A deviation with respect to the ideal case: the considered case features a curved surface with the possibility of sustained stream-wise vortex structures. (ii) The case is not homogeneous in spanwise direction, so that large-scale structures generated by some instability may synchronize in space, so that they persist in the average. Phase averaging requires long transient simulations, which are very costly. For this reason, the temporal extent of simulations is limited. To account for these fluctuations, we relax the suggested eigenvalue configuration to $1 < \max[\lambda_1, \lambda_2]$.

The treatment of Condition 3 is straightforward, as we now only require an inward flow pattern that is not necessarily radial.

As a result, a modified anti-splat condition is defined in order to capture the wake impact:

2. $\forall (\mathbf{x}_0, t_0) \in S_R$: a fluid parcel moving backward in time toward B along trajectory $s_{\mathbf{x}_0, t_0} : T \rightarrow S_R$ is stretched in one tangential direction parallel to B and compressed in normal direction
3. There exists a closed curve in $S_R \cap (B^c \times T)$ with an inward oriented flow pattern.

Note that the previously defined anti-splat definition is a subset of the new relaxed anti-splat definition. In the following, we refer to this modified definition as wake impact and the associated detection method as wake impact detection.

7.4 Wake impact associated perturbation

In addition to detecting the periodic wake impact, our goal is to link it to the perturbation of the boundary layer. We do this by introducing a perturbation threshold \hat{d} limiting the streamlines we include for the modified anti-splat definition. The computation of the right Cauchy–Green deformation tensor is only performed for streamlines, where every point of the streamline is related to a perturbation above the perturbation threshold. By doing this, the detected wake impact region is guaranteed to be associated with a specified minimal flow perturbation.

7.5 Scale of the wake impact

In our previous work, splats and anti-splats were introduced as usually small-scale flow features in turbulent flows, which we detected at wall level with a slight offset. This was done by computing the trajectories backward in time starting from the control points located on an offset surface $\mathbf{x} \in B^\epsilon$. These trajectories were then used to compute the deformation tensor.

In contrast, the wake impact is a large-scale feature in the periodic contribution. When considering wall level anti-splats by choosing a small ϵ , as we suggested in our previous work, we only detect a sub-region of the wake impact and lose the ability to evaluate the penetration depth of a wake in a meaningful way. The anti-splat detection is sensitive to the ϵ -value. As a result, finding a large enough but suitable ϵ that captures the complete anti-splat in the present case is challenging and cumbersome.

We resolved this issue by not selecting a single offset ϵ , but a maximum offset $\hat{\epsilon}$ and a resolution. Based on the input grid, the resolution, and the maximum offset $\hat{\epsilon} \in \mathbb{R}$, we can select a set of offset surfaces $\{B_0^\epsilon, B_1^\epsilon, \dots, B_n^\epsilon\}$. In the following, we perform the anti-splat detection method for every offset surface individually.

7.6 Modifications to the detection algorithm

Region growing

Previously (Nsonga et al. 2020), we computed the deformation tensor for every point of the offset surface and applied the anti-splat criteria accordingly, which resulted in a binary field. We used this binary field to apply a region growing scheme in order to find disjoint regions. The regions were then tested for a radial flow pattern by searching for a sink in a tangential velocity field of the offset boundary surface. This approach corresponds to first testing for Condition 2, then imply Condition 1 by region growing, and then testing for Condition 3. As testing for Condition 3 is the final step, previously computed regions can be discarded.

We now optimized this approach by first locating critical points in the tangential velocity field of the offset boundary surface in accordance with the modified anti-splat Condition 3. The enclosing control points of the boundary surface are then used as seed points. We then apply a flood fill approach, recursively evaluating the deformation tensor at the adjacent vertices. As a result, we limit the numerical integration and evaluation of the deformation tensor to points which are likely to be part of an anti-splat region.

Curved surfaces

The (anti-)splat detection algorithm is designed for flat surfaces. Previously, we transformed the data from the curvilinear physical domain into a uniform computational domain before applying the detection algorithm (Nsonga et al. 2020).

Here, we optimize this step by bypassing the domain transformation and locally applying a domain transformation while computing the gradient. When computing the spatial gradient, the local coordinate system is rotated so that the first basis vector is in the tangential component of flow and the second basis

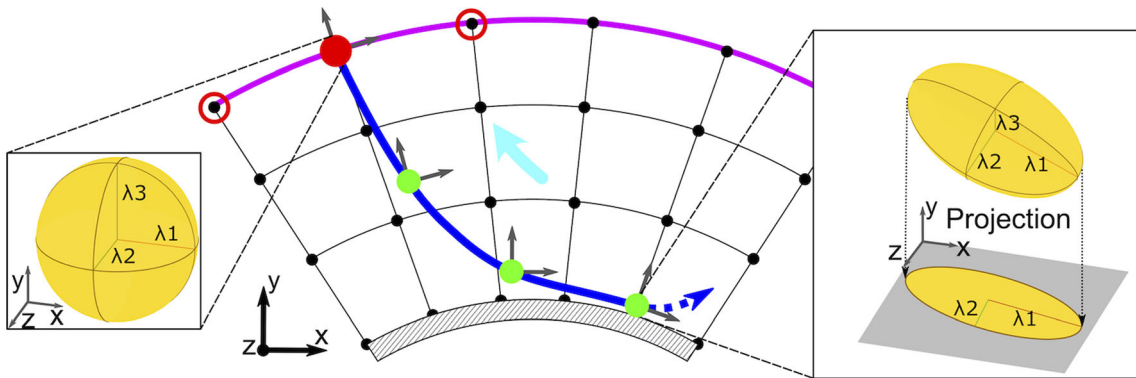


Fig. 7 Illustration of the wake impact detection method for curvilinear grids. This image includes a seed point \mathbf{x}_s (red) with the adjacent seed points (red circles) in a specific offset surface B_i^ϵ (purple). Also, the streamline with its direction of integration (blue) under the abort criterion with its sample points $\{s_0, s_1, \dots, s_{N-1}\}$ (green) is shown. The direction of the underlying flow is also displayed (cyan) (cf. Sect. 8)

vector is equal to the wall-normal. It is straightforward to compute a third vector to construct an orthonormal basis. This approach is equivalent to a concurrent domain transformation within the original data (cf. Fig. 7).

8 Wake impact detection algorithm

8.1 Detection algorithm

With the input parameter $\hat{\epsilon}$, we construct a curvilinear grid $G_B \subset G$, where G is the input grid. The subgrid G_B is bounded by the boundary surface, the offset surface with the highest ϵ -value, the leading edge, and the trailing edge of the turbine blade. The number of offset surfaces corresponds to the number of slices of the input grid within the bounds. In highly resolved data, it is reasonable to reduce the number of offset surfaces used through a slice spacing $r \in \mathbb{N}$ to reduce computation time. This determines the spacing between two offset surfaces by removing intermediate offset surfaces.

For all elements of the set of offset surfaces $\{B_0^\epsilon, B_1^\epsilon, \dots, B_n^\epsilon\} \subset G_B$, we compute the tangential velocity $\tilde{\mathbf{u}}_t(\mathbf{x}, \phi)$ and compute cell locations of the critical points $\{\mathbf{x} \in D : \|\tilde{\mathbf{u}}_t(\mathbf{x}, \phi)\| = 0\}$. The control points of the grid cell locations are the initial seed points for the wake impact detection.

For every seed point $\mathbf{x}_s \in B_i^\epsilon$, we perform a numerical integration backward in time. Every phase is analyzed individually as stated in Sect. 5, so the flow field of a phase is treated as steady. Hence, when referring to time here, this is a pseudo-time alluding to motion along the frozen streamline in the respective phase.

In order to capture the advection and, therefore, deformation of a fluid volume moving toward the boundary, an abort criterion was introduced in Nsonga et al. (2020). Here, we combine this with our considerations from Sect. 7.4, by additionally applying the perturbation threshold:

$$\forall \mathbf{x} \in s_{\mathbf{x}_0, t_0} : \tilde{\mathbf{u}}(\mathbf{x}, \phi) \cdot \mathbf{n}(\mathbf{x}) \geq 0 \wedge \hat{d} < d(\mathbf{x}, \phi). \quad (6)$$

Note, that we do not set a maximum integration time, as Eq. 6 reliably aborts the integration and includes the complete near-wall wake region associated with a specific minimal perturbation. Along this streamline, a list of sample points $\{\mathbf{s}_0, \mathbf{s}_1, \dots, \mathbf{s}_{N-1}\}$ equidistant in pseudo-time approximating the streamline is extracted. The temporal distance between two sample points Δ_t is set by the user.

The following computation of the deformation tensor requires the spatial gradient of the phase contribution at the sample points: $\nabla \tilde{\mathbf{u}}(\mathbf{s}_i, \phi)$. We estimate the spatial gradient using a central difference scheme with negated velocities to account for anti-splats and a first-order forward or backward scheme at boundaries. We rotate the orthonormal basis and the velocity vectors used for the computation of the spatial gradient according to the considerations in Section 7.6 utilizing a rotation matrix $R(\mathbf{x}) \in \mathbb{R}^{3 \times 3}$. The spatial gradient in a tangential reference frame is denoted as: $\nabla_R \tilde{\mathbf{u}}(\mathbf{s}_i, \phi)$.

We then compute the right Cauchy–Green tensor $C(\mathbf{x}_s, \phi)$ to evaluate the fluid volume deformation:

$$C(\mathbf{x}_s, \phi) := \Psi(\mathbf{x}_s, \phi)^T \Psi(\mathbf{x}_s, \phi), \quad (7)$$

with $\Psi(\mathbf{x}_s)$, a gradient computed according to localized FTLE (Kasten et al. 2009):

$$\Psi(\mathbf{x}_s, \phi) := \prod_{i=N-1}^0 \exp[\Delta_t \nabla_R \tilde{\mathbf{u}}(\mathbf{s}_i, \phi)]. \quad (8)$$

The change of the reference frame allows to interpret the deformation process along a curved surface as a deformation process on a flat surface. In this case, the tangential reference plane is spanned by the reference vectors $\mathbf{t}_1 = [1, 0, 0]^T$ and $\mathbf{t}_2 = [0, 0, 1]^T$. We use the reference normal $\mathbf{n} = [0, 1, 0]^T$. With the projection matrix $M := [\mathbf{t}_1 \ \mathbf{t}_2] \in \mathbb{R}^{3 \times 2}$, this results in a tangential deformation tensor $C_t(\mathbf{x}_s, \phi) = M^T C(\mathbf{x}_s, \phi) M$ and a normal deformation tensor $C_n(\mathbf{x}_s, \phi) = \mathbf{n}^T C(\mathbf{x}_s, \phi) \mathbf{n}$.

Analyzing the tangential and the normal deformation individually allows to characterize the flow volume behavior in terms of the wake impact according to Condition 2 in Sect. 7.3. It is fulfilled if,

$$\lambda_{\max}[C_t(\mathbf{x}_s, \phi)] > 1 \wedge C_n(\mathbf{x}_s, \phi) < 1, \quad (9)$$

where $\lambda_{\max}[\cdot]$ denotes the maximum eigenvalue. If the condition is fulfilled, we recursively repeat the process of numerical integration and evaluation of the deformation tensor for all adjacent points in the offset boundary B_i^ϵ . The algorithm is illustrated in Fig. 7.

Initializing a set of functions $\chi_i : B_i^\epsilon \times \mathbb{R} \rightarrow \{ \text{true}, \text{false} \}$ as false, and setting $\chi_i(\mathbf{x}_s, \phi)$ true if the wake impact conditions are fulfilled, we obtain a set of binary fields. These fields are the input for our new visualization approach introduced in Sect. 9.

8.2 Implementation details

For the numerical integration we employed the Dormand–Prince method (Dormand and Prince 1980). To improve the performance of the recursive algorithm, we implemented it as an iteration using a Last-In-First-Out stack. The stack is initialized with all seed points \mathbf{x}_s from all offset surfaces. The neighbors of a seed point belonging to the wake impact are pushed in the stack. We then use OpenMP Tasking to process the stack in parallel by spawning a Task for every seed point read from the thread-safe stack. The tasks are dynamically scheduled and run in parallel. As the reading/writing only takes a fraction of the computation time, and the integration combined with the computation of the deformation tensor is highly asynchronous, bottlenecks are not problematic.

8.3 Detection parameters

Maximum offset distance $\hat{\epsilon}$ and spacing r

For the reasons discussed in Sect. 7.5, the maximum offset distance must be sufficiently high to capture the large-scale wake impact. It should also be outside of the presumed boundary layer, as our goal is to capture the penetration of the wake impact. For this case study, we found a maximum offset distance $\hat{\epsilon} = 0.1c_{ax}$ to be sufficient.

Due to the high resolution of the original grid, neighboring offset surfaces have substantially overlapping functions $\chi_i(\mathbf{x}_s, \phi)$. Here, we use the slice spacing $r = 2$. As a result, we only use every second offset surface for the computation. This improves computation time without affecting the resulting visualizations.

Step size Δ_t

As in our previous approach, the step size determines the frequency at which the gradient field is sampled. A low frequency leads to artifacts due to aliasing. To ensure that a streamline produces at least one sample point in every cell it passes through, we compute an upper bound for the step size (Equation 19 in Nsonga et al. (2020))

$$\Delta_+ = \frac{1}{2} \frac{\min \{ \Delta_i; \Delta_j; \Delta_k \}}{\max \| \bar{\mathbf{u}}(\mathbf{x}, \phi) \|}, \quad \mathbf{x} \in G_B \quad (10)$$

with the grid point spacing $\{ \Delta_i; \Delta_j; \Delta_k \}$ of the cells of G_B . This corresponds to a Courant–Friedrichs–Lewy condition with a Courant number of 0.5. Applying this to the input velocity field in phase $\phi = 15/40$ with the minimum grid point spacing $\min \{ \Delta_i; \Delta_j; \Delta_k \} = 1.76 \cdot 10^{-4} c_{ax}$ and $\max \| \bar{\mathbf{u}}(\mathbf{x}, \phi) \| = 1.57 \cdot 10^{-1} U_{ref}$, results in an upper bound $\Delta_+ = 1.11 \cdot 10^{-3} c_{ax} / U_{ref}$. Based on this computation, we selected a step size of $\Delta_t = 1 \cdot 10^{-3} c_{ax} / U_{ref}$ in pseudo-time.

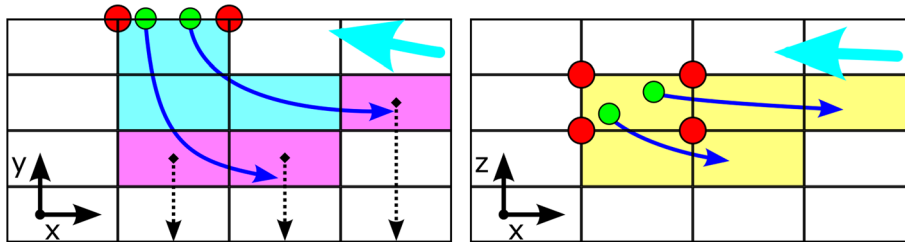


Fig. 8 Illustration of the penetration depth visualization scheme for the boundary surface in terms of a side view (*left*) and a top view (*right*). These images include seed points $\mathbf{x}_s : \chi_i(\mathbf{x}_s, \phi) = \text{true}$ (*red*), the streamline with its direction of integration (*blue*), and $M = 2$ sample points (*green*). The direction of the underlying flow is also displayed (*cyan arrow*). The y^+ -value at a specific cell center (*purple*) are projected onto the corresponding boundary cells (*yellow*)

9 Visualization of penetration depth

9.1 Visualization algorithm

Focusing on an intuitive visualization scheme, we found a 2D color-mapping of the penetration depth on B to be most viable. For this purpose, we define a volume approximation of the wake impact such that all points within this 3D region have a perturbation higher than the threshold.

Volume approximation

As our detection algorithm finds connected regions on the offset surfaces, we can interpret these regions as wall-parallel 2D cuts of the wake impact volume. The idea is to approximate the volume by integrating a sufficient number of streamlines backward in pseudo-time, starting within these 2D cuts. We can then construct a binary field defined on G_B by capturing which cells of the grid G_B were penetrated by an arbitrary streamline seeded within a 2D cut. In practice, we obtain quad patches for every offset surface B_i^ϵ . The four control points of a quad patch must all belong to the wake impact region. With the control points as outer bounds, we compute M seed points at random positions, where $M \in \mathbb{N}^+$ is a user defined sample number. These are then used for the numerical integration, as illustrated in Fig. 8, with the same abort criterion as in the detection method (Eq. 6).

Boundary projection

To visualize the deepest penetration, we first identify the cells of the wake impact volume with the lowest distance from the wall. As G_B is a structured grid, this is straightforward. We obtain a cell at every index pair (i, j) associated with the x - z plane.

The grid resolution limits the accuracy of the volume approximation. To find an appropriate y^+ -value of a cell in the approximation, we compute the mean y^+ -value of the cell vertices. These values are then projected onto the boundary surface B according to Fig. 8. We then apply a cell-based color mapping of the y^+ -values.

To provide high expressiveness and nameability of the graphs addressing the penetration of the perturbation associated wake-impact into the near-wall flow, we apply a colorful colormap. Focusing on nameability, Reda et al. (2021) show the benefits of incorporating colorfulness and nameability in the visualization design process.

Stagnation line

In addition to the penetration depth, the described visualization algorithm allows to characterize the center of the wake. It is defined as the set of points with no tangential velocity closely above the wall and termed stagnation line. Its evaluation is performed as follows.

We compute the tangential velocity at every step during the integration, starting at the sample points, as shown in Fig. 8(left). The tangential velocities are then assigned to the corresponding cell of the grid G_B . We perform these steps in conjunction with the Volume approximation. After computing the average of the corresponding tangential velocities for every cell, we project the values onto the boundary in an analogous procedure for the Boundary projection described above.

Once the velocities have been projected, the stagnation line is taken as the position where the tangential velocity changes its sign between projected cell neighbors. In this step, we disregard the z -component of the velocity due to the nature of the present case, as the sought stagnation line should be approximately parallel to the z -axis, but this can be generalized. In the visualization, each point found in this way is represented through a black bar. This procedure is highly flexible and can yield a single line but also multiple lines, if the condition is met, as seen before.

9.2 Visualization sample number

Increasing the sample number M increases the accuracy of the volume approximation at the cost of computation time. To find a sufficiently high value for M , we increase it and observed how many boundary cells are found (cf. purple cells in Fig. 8), with the result displayed in Fig. 9. A plateau is evident, suggesting that increasing M beyond a threshold does not affect the results significantly. We found a sample number $M = 50$ to be appropriate for this case. Other values might be found suitable by the reader, depending on the available hardware and the situation considered.

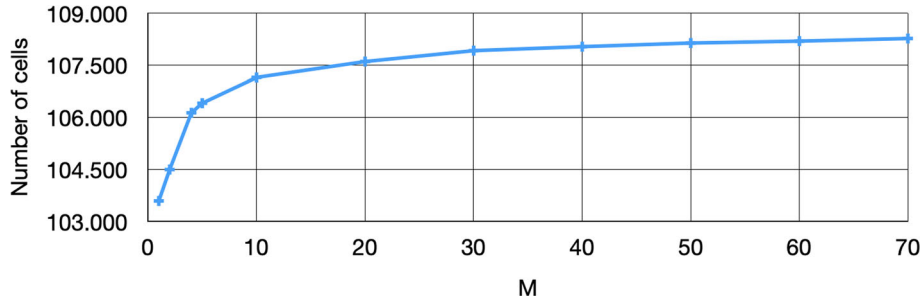


Fig. 9 The number of boundary cells associated with a wake impact plotted against the number of sample points M used for the volume approximation in our visualization scheme

10 Comparison and performance

10.1 Comparison to anti-splat detection

The previous method in Nsonga et al. (2020) applies anti-splat detection after a domain transformation. Here, we map the resulting anti-splat regions into the physical domain and apply the new visualization scheme.

In contrast to our wake impact detection method, the anti-splat detection method requires to set the maximum integration time τ and a single offset distance. As discussed earlier in Sect. 7.5, finding an appropriate offset distance is not straightforward. For this comparison, we used various offset distances below the set maximum offset distance $\hat{\epsilon}$. In contrast to the previous approach, the integration of the new method is reliably aborted by the criterion Eq. 6 in the present case. Comparing the previous method and the new one requires to fix an integration time for the former. To determine an appropriate value, we analyzed the maximum integration times at which the abort criterion interrupts the integration in the new method. We found a median of integration times of $\tau = 0.9$ with the first quartile at $\tau = 0.45$ and third quartile at $\tau = 1.6$, so that an integration time of $\tau = 1$ seems reasonable to conduct a comparison between the two methods.

The results in Fig. 10 demonstrate the usefulness of the modified scheme. The (anti-)splat detection method is sensitive to the offset distance. The new wake impact detection method can reliably detect the wake impact without manually exploring the parameter space to find suitable offset distances. Also, the previous (anti-)splat method finds disjoint anti-splat regions instead of a continuous wake impact structure.

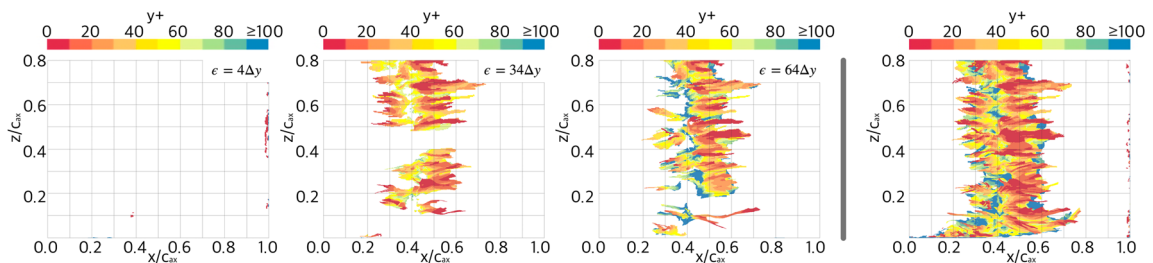


Fig. 10 Comparison between the previous (anti-)splat detection method with a single offset plane and the current detection of wakes. The first, second, and third image show the result of the splat detection for various offset distances of 4, 34, and 64 control volumes away from the wall, respectively, using the same integration time of $\tau = 1c_{ax}/U_{ref}$. The fourth picture shows the new volume-based method. The detected anti-splat regions of both methods are visualized according to Sect. 9 with a perturbation threshold of $\hat{d} = 5\%$. Results correspond to phase 15/40

10.2 Performance

The following computation times were obtained on a Linux system with Ubuntu 18.04 LTS, 32GB of RAM, and an Intel(R) Xeon(R) CPU E5-2630 v3 @ 2.40GHz chip (2 physical processors and 32 threads).

Detection runtime

We measured the run time of the anti-splat detection and wake impact detection for phase $\phi = 15/40$ with the parameters fixed in the previous subsection and $\hat{d} = 5\%$. The wake impact detection with the maximum offset range of $\hat{\epsilon} = 0.1c_{ax}$ includes 96 offset surfaces. With the resolution factor $r = 0.5$, we obtain 48 offset surfaces. The computation time for all surfaces is 19:25 min or approximately 24 s per slice on average. The previously proposed anti-splat detection with the sample offset distances 4, 34, 64, and 94 control volumes away from the wall required 51 s, 58 s, 62 s, and 72 s, respectively. On average, it required approximately 60 s per slice.

Visualization runtime

The computation time of the visualization depends on the number of detected seed points and the parameter M and scales linearly. For the applied sample number $M = 50$, the computation required 22:14 min. For comparison, sample numbers $M = 1, 20, 40$, and 60 required 0:30 min, 8:58 min, 17:47 min, and 26:54 min, respectively.

11 Results and discussion

11.1 Periodic wakes on pressure side

The “negative jet” structure results from the low momentum of the incoming wakes reaching the pressure side (PS) of the turbine blade. Due to the direction of this contribution to the flow field, the impinging wake extracts low momentum from the blade boundary layer into the passage region. To visualize the “negative jet”, we apply the new detection method to individual periodic fluctuation fields $\tilde{\mathbf{u}}(\mathbf{x}, \phi)$ for each individual phase ϕ with the previously derived parameters.

Results for four phases are presented in Fig. 11 showing a 3D view of streamlines based on the periodic contribution $\tilde{\mathbf{u}}(\mathbf{x}, \phi)$. Clearly, the wake impact fulfills the relaxed anti-splat condition, and through this detection algorithm, the wake is identified. The visualization unambiguously depicts the region where the flow from near the blade is extracted toward the middle of the passage. Even more, it provides a systematic approach for detecting and visualizing this flow structure and, hence, is suitable for regions where the flow structure is complex, i.e., the corner between the blade and the endwall. Figures 10 and 11 reveal that in phase 15/40 the wake close to the endwall lags behind the main wake. It is particularly this ability of the proposed scheme to unambiguously and seamlessly define the wake impact in such a situation with large distortion that makes the visualization method interesting for the domain experts. The characteristics observed in the 2D cutplane can also be hinted at in this figure. For instance, the two recirculation zones just above the wake impact zone, depicted in Fig. 3, can be deduced. Yet, they do not belong to the anti-splat and hence, to the wake impact, as these are not responsible for shifting flow away from the blade.

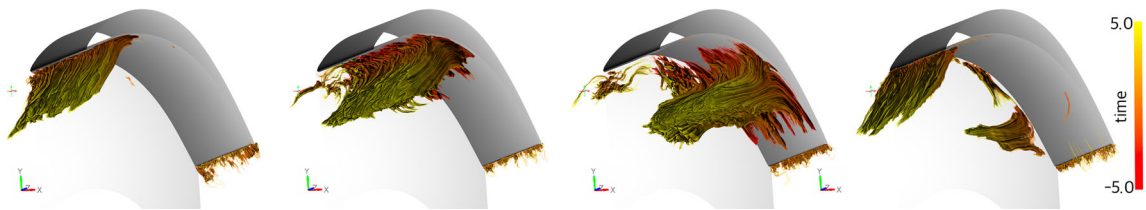


Fig. 11 Streamline visualization of the wake impact detected with the present method. From left to right the phases $\phi = 5/40, 15/40, 25/40, 35/40$ are displayed. Starting at the seed points \mathbf{x}_s (cf. Fig. 8), streamlines are integrated backward in time with respect to the abort criterion in Eq. 6 with a perturbation threshold $\hat{d} = 5\%$ as well as forward in time. Here, the integration time is limited to $5c_{ax}/U_{ref}$

11.2 Friction coefficient

The friction coefficient characterizes the losses due to viscous friction at the wall and also provides a means to infer the boundary layer state, although not unambiguously. Figure 12 presents the friction coefficient determined using the phase averaged flow, $\bar{c}_f = \bar{\tau}_w / (1/2 \rho u_\infty^2)$. The presented value of c_f is the average over $z/c_{ax} \in [0.2; 0.8]$. This spanwise region is denoted as the blade center region. The region below is considered as the region under the influence of secondary flows, which are due to the presence of the endwall at $z = 0$. In the figure, arrows denote the position of the wake stagnation line. The local minimum at $x \approx 0.16c_{ax}$ observed for all phases would suggest transition to turbulence. However, considering other statistical quantities, here not discussed for the sake of brevity, indicate that the boundary layer does not become fully turbulent. This is supported by Michelassi et al. (2003), who, in a case with a higher Reynolds number than the current one, found that the boundary layer was not fully turbulent for the present configuration.

Furthermore, the second local minimum at $x \approx 0.55c_{ax}$ in phase 15/40 is related to the wake. In this phase, the stagnation line of the wake on the blade is located around $x = 0.4c_{ax}$. As the wake impact is an anti-splat, the upstream part of the wake causes an acceleration of the flow, hence the local maximum at $x = 0.3c_{ax}$ in Fig. 12. Downstream of the stagnation line, the wake is slowing down the flow. Using the friction coefficient is a standard approach to characterize the effect of the wake on the boundary layer. However, it is restricted to the two-dimensional wall itself. By the proposed visualization, the interaction of the wake with the whole boundary layer and even further can be addressed, that is in a volumetric way.

11.3 Wake perturbation of the boundary layer

Our proposed visualization scheme enables characterizing in detail how the wake interacts with the boundary layer. Figure 13 presents for four different phases how close to the blade surface perturbations reach. This distance to the wall is coded in the figure in terms of wall units. This enables identifying where the wake perturbations reach deeper in the boundary layer. The last row presents the level of periodic perturbation $d(\mathbf{x}, \phi)$, but extracting the information at a plane parallel to the wall at a defined distance. This would be a typical approach to date. The advantage of the present method is the ability to systematically consider the wake-related effects only and filter them in terms of wall distance and perturbation level.

Phase $\phi = 5/40$

Starting with the phase where the wake impacts just downstream of the LE, in general, only small perturbations are caused by the wake, up to around 5% in the center region. Furthermore, these are highly asymmetric, with perturbations by the upstream leg of the wake being very small. This reduced level of perturbations can be related to the flow acceleration at the LE. Furthermore, these perturbations only rarely reach the boundary layer regions where viscous effects are most dominant, i.e., only in a few positions is the boundary layer perturbed below $y^+ = 10$. In the center region, the trajectories of the perturbations remain at constant spanwise positions, $z = \text{const}$. In contrast, next to the endwall, the wake causes high perturbations, and the trajectories do not remain at constant spanwise position, revealing a complex 3D interaction.

Phase $\phi = 15/40$

In the next phase, the perturbation caused by the wake is markedly stronger. Furthermore, strong perturbations reach positions deeper inside the boundary layer, frequently reaching $y^+ < 10$. In contrast to the previous phase, there is a certain symmetry with respect to the wake stagnation line. Both upstream and

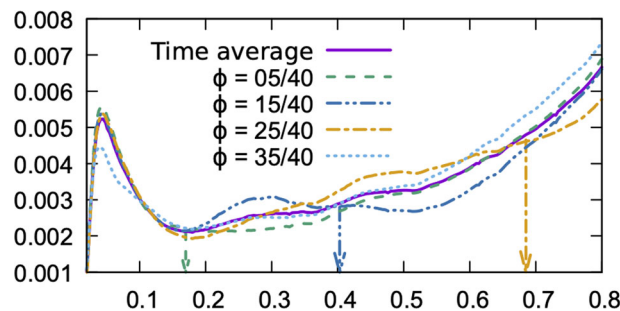


Fig. 12 Friction coefficient c_f along the x -coordinate at the pressure wall for four different phases together with the fully time averaged value. The data were obtained by averaging in z -direction over $z = 0.2 \dots 0.8$. Arrows denote the position of the wake stagnation line for each phase using the same line style

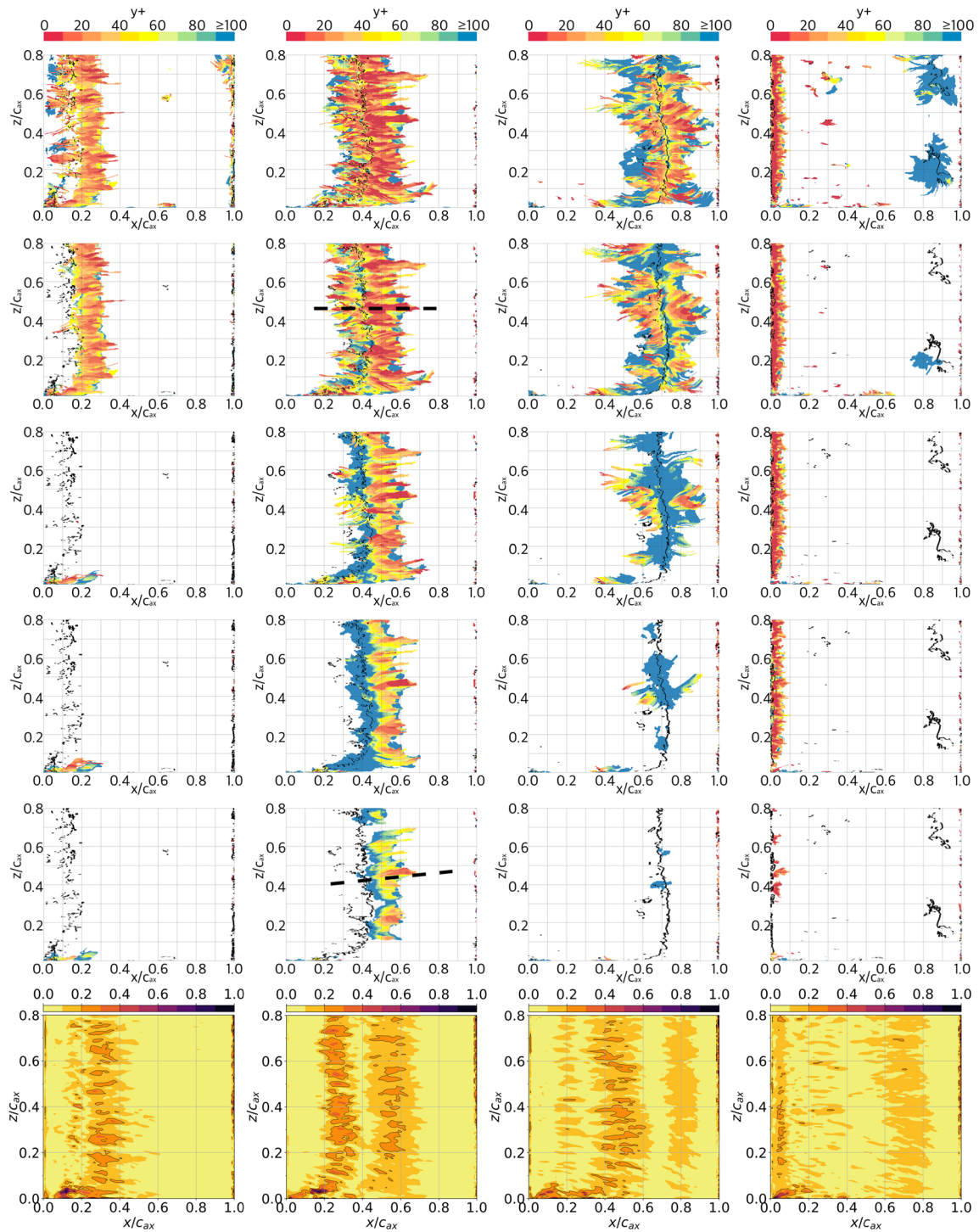


Fig. 13 Minimum distance from the wake impact volume approximation to the blade pressure side. From left to right, four phases are shown $\phi = 5/40, 15/40, 25/40, 35/40$. Various disturbance thresholds are applied. From top to bottom (except last row) the minimum distances above the perturbation thresholds $\hat{d} = 3\%, 5\%, 7\%, 9\%$ and 11% are displayed. Note that the stagnation lines shown correspond to $\hat{d} = 3\%$ and are the same in all graphs of a column. The last row presents the perturbation $d(\mathbf{x}, \phi)$ in a wall-parallel plane located two control volumes away from the wall ($\Delta n = 0.0016c_{ax}$) for all four phases

downstream leg perturb the boundary layer, although trajectories of the downstream leg are longer. Furthermore, while small fluctuations $\hat{d} < 5\%$ reach down to regions dominated by viscosity effects for both upstream and downstream legs, higher fluctuations show a difference. The downstream leg perturbs the

inner part of the boundary layer strongly, while the upstream leg only affects the external part of the boundary layer. A change in the trajectories can also be noted. For the two smaller perturbation levels, trajectories remain at constant spanwise locations (see the black dashed line at $\hat{d} = 5\%$). Contrarily, trajectories associated with stronger perturbations do not; they present a slight tendency to move in positive z -direction.

Let us now consider the perturbation field of this phase in a plane at a constant distance from the PS wall, the last row in Fig. 13. The stagnation line agrees very well with the splat streamlines for very low y^+ values (they denote similar positions). Of notice is that in this plane, the highest perturbations are observed upstream of the stagnation line, while the splats streamlines indicate that the highest perturbations occur downstream. Furthermore, the observed region of perturbation upstream of the splat line ($0.2 \lesssim x/c_{ax} \lesssim 0.35$) in this plane is larger than what is depicted through the wake impact $0.25 \lesssim x/c_{ax} \lesssim 0.4$. This apparent contradiction can be explained as follows. The condition set to define the wake impact, Eq. 6, involves the flow deviating from blade tangential to blade normal. Furthermore, for visualization, a condition on the perturbation strength throughout the streamlines resulting from the anti-splat detection must be above a given threshold. Looking at the phase perturbation in Fig. 3, at $x/c_{ax} \approx 0.3$ the flow is tangential to the blade. Hence, at this position, the backward integration in the anti-splat algorithm stops. This is a consequence of the anti-splat definition, which here serves to characterize the region of the wake extracting flow from the blade toward the passage center. Concerning the perturbation level, near the wall velocities are very small. Hence, small changes can lead to high relative perturbation levels locally. In the current algorithm, streamlines are considered as long as the perturbation level is above a given threshold. Therefore, comparing the results from the wake impact and the perturbation in the last row in Fig. 13, it can be deduced that the perturbation levels shown in the last row are localized and that overall the perturbation levels are assessed to be smaller than by the proposed wake impact representation, which seems to be more realistic.

Phase $\phi = 25/40$

Advancing to the next phase, trajectories are more slanted, evidencing a more complex interaction, which can be addressed by 3D visualizations like in Fig. 11. The method proposed here specifically links the near-wall flow to the flow further away from the wall by defining a true volume with connected behavior. Furthermore, while the visualization of the perturbation at a plane near the PS wall, displayed in the last row in the figure, would indicate a symmetric alteration of the boundary layer by the wake, the trajectories belonging to the wake, shown in the third row, reveal a different structure. Here, a similar situation as in the previous phase is found, where the wake impact, which is shifting flow from near the blade toward the passage, has a smaller footprint upstream of the stagnation line than the perturbations seen in a plane next to the wall.

The current wake impact visualization reveals a complex interaction of the wake and the boundary layer in this phase. Small perturbations reach the inner parts of the boundary layer, mostly near the stagnation line. Furthermore, both upstream and downstream legs are similarly affected. Contrarily, stronger perturbations show a different structure, as seen with $\hat{d} \geq 5\%$. Near the stagnation line, the outer part of the boundary layer is affected. Yet, away from the stagnation line, these perturbations reach much deeper into the boundary layer.

Phase $\phi = 35/40$

Concluding with the phase where the wake is about to reach the TE, the boundary layer is perturbed superficially and with low intensity. In contrast, the usual representation (last row) would indicate a marked effect of the wake. Yet, as no wake trajectories reach deep within the boundary layer, the perturbations observed in the last row for this phase do not belong to the direct wake impact but are remainders from the passing wake close to the wall. The observed perturbation levels are smaller in successive planes away from the blade wall. Finally, the wake impact visualization shows that the fairly two-dimensional wake seen in earlier phases has disintegrated and lost its overall coherence. In this phase, only two weak anti-splat-like spots are identified. This shows the ability of the method to seamlessly change from a 2D wake impact to a more or less axisymmetric impact, a feature highly relevant for applications.

11.4 Assessment

When introducing a new tool, it is best to compare it with what is available. Figure 14 shows a picture of an earlier publication of the domain experts involved in the present research using classical visualization methods, with much effort spent on optimizing the presentation. The grey scale displays the energy of the wall-parallel fluctuations close to the wall, which is similar to the last row of Fig. 13. This information is

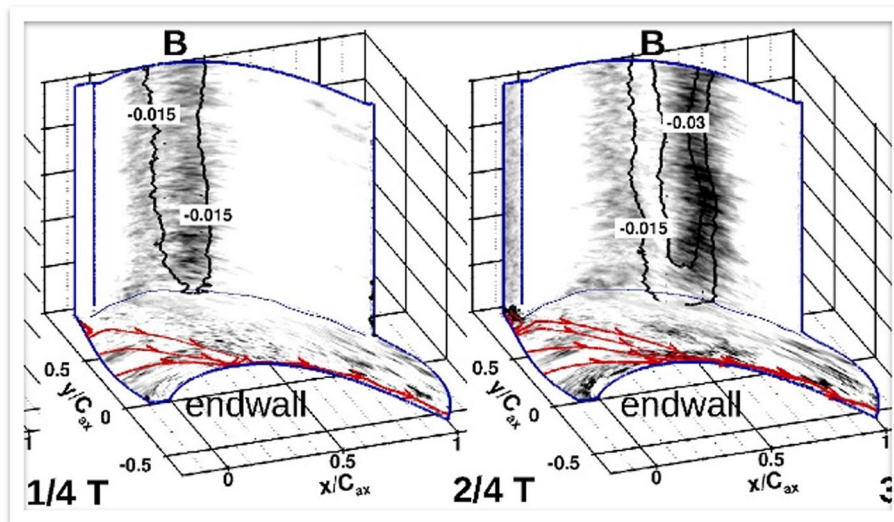


Fig. 14 Extract of Fig. 12 from an earlier publication of the domain experts (Koschichow et al. 2014) with conventional visualization techniques. Reprinted with the permission of ASME

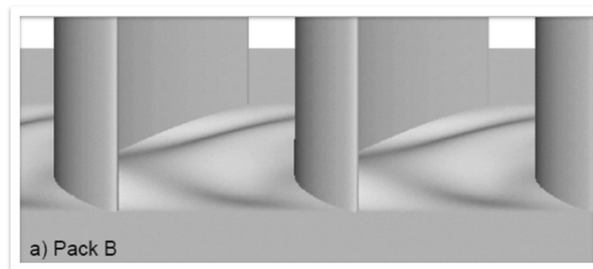


Fig. 15 Example of endwall contouring of a low-pressure turbine blade. Extract of Fig. 8 from Praisner et al. (2007). Reprinted with the permission of ASME

limited to the wall, as discussed, and does not provide any fluid mechanic assessment, like the degree of perturbation of the boundary layer. Furthermore, and most importantly, little information on the distortion of the wake in the corner is visible, and three-dimensional volumetric information, as shown in Fig. 11 is not available at all. The new scheme, hence, constitutes a substantial achievement. Once the volume of the impinging wake is determined, conditional averages can be computed to assess the contribution of this feature to overall dissipation, for example. Another advantage of extracting and understanding the unsteady impinging wake in a turbine cascade, particularly near the wall, is understanding their interaction with sidewall contouring. Sidewall contouring is an approach to optimize performance by modifying the contour to accommodate stationary secondary flows, shown in Fig. 15. Unsteady wakes are not considered for this, but it has to be assessed to which extent their effect is improved or aggravated. Visualization, analysis of strength, and conditional average over the respective volume constitute options now available.

12 Conclusions

An algorithm for the detection and visualization of anti-splats has been extended and applied to the flow along the pressure side of a low-pressure gas turbine blade under the effect of periodically incoming wakes. We generalized a previously proposed detection algorithm to be directly applicable to curvilinear grids while making it more efficient and robust against parameter selection. In contrast to previous applications, we considered the periodic contribution generated by the regular perturbation of the mean flow, yielding an anti-splat continuously moving along the boundary of the computational domain.

It was shown that the wake impinging on the pressure side of the turbine stage fulfills the condition of a relaxed anti-splat structure. The resulting structure has been visualized through streamlines. Due to the periodic nature of the interaction of wakes with the turbine blade, phase averaged velocity fields were used. It was possible to assess how far into the boundary layer a certain perturbation level can reach through the obtained streamlines. This was achieved by evaluating the minimum distance of the anti-splat streamlines to the wall. A physical interpretation has been performed through a non-dimensional distance to the wall, y^+ .

The current method has enabled visualizing the complex and 3D interaction of the wakes with the boundary layer. Additionally, it has enabled us to characterize the position of the stagnation line of the wake impact. Lastly, the complex interaction between wake and secondary flows near the endwall is also captured. This is evidence for the robustness of the method in handling flow configurations that deviate markedly from the ideal case and cannot be addressed in the same way by other methods. Hence, the proposed concept provides a consistent and sound basis for evaluation, even in such complex situations, which domain specialists highly desire.

We will extend the (anti-)splat detection technique to unstructured arbitrary grids in the future. The application specialists would like to combine the tool with a more in-depth analysis of the boundary layer itself and employ it for other similar cases of wake-blade interactions, like different cases of turbine cascades and flows in compressor cascades.

Acknowledgements This work was funded by the German Federal Ministry of Education and Research within the project Competence Center for Scalable Data Services and Solutions (ScaDS) Dresden/Leipzig (BMBF 01IS14014B). JF and JVM acknowledge funding by DFG under FR1593/15-1 within PAK948.

Funding Open Access funding enabled and organized by Projekt DEAL.

Declarations

Conflict of interest The authors declare that they have no conflict of interest.

Open Access This article is licensed under a Creative Commons Attribution 4.0 International License, which permits use, sharing, adaptation, distribution and reproduction in any medium or format, as long as you give appropriate credit to the original author(s) and the source, provide a link to the Creative Commons licence, and indicate if changes were made. The images or other third party material in this article are included in the article's Creative Commons licence, unless indicated otherwise in a credit line to the material. If material is not included in the article's Creative Commons licence and your intended use is not permitted by statutory regulation or exceeds the permitted use, you will need to obtain permission directly from the copyright holder. To view a copy of this licence, visit <http://creativecommons.org/licenses/by/4.0/>.

References

- Berrino M, Lengani D, Simoni D, Ubaldi M, Zunino P, Bertini F (2015) Dynamics and turbulence characteristics of wake-boundary layer interaction in a low pressure turbine blade. In: Turbo expo: power for land, sea, and air, vol. volume 2A: turbomachinery. <https://doi.org/10.1115/GT2015-42626>. V02AT38A014
- Bhatia H, Pascucci V, Kirby RM, Bremer P-T (2014) Extracting features from time-dependent vector fields using internal reference frames. In: Proceedings of the 16th Eurographics conference on visualization. EuroVis '14, pp 21–30. Eurographics Association, Goslar, DEU
- Bujack R, Yan L, Hotz I, Garth C, Wang B (2020) State of the art in time-dependent flow topology: interpreting physical meaningfulness through mathematical properties. *Comput Graph Forum* 39(3):811–835. <https://doi.org/10.1111/cgf.14037>
- Busse P, Krug A, Vogeler K (2014) Effects of the steady wake-tip clearance vortex interaction in a compressor cascade: part II—numerical investigations. In: Turbo expo: power for land, sea, and air, vol. volume 2A: turbomachinery. <https://doi.org/10.1115/GT2014-26121>. V02AT37A031
- Cardamone P, Stadtmüller P, Fottner L (2002) Numerical investigation of the wake-boundary layer interaction on a highly loaded LP turbine cascade blade. In: Turbo expo: power for land, sea, and air, vol. volume 5: turbo expo 2002, parts A and B, pp 401–409. <https://doi.org/10.1115/GT2002-30367>
- Chapman GT, Yates LA (1991) Topology of flow separation on three-dimensional bodies. *Appl Mech Rev* 44(7):329–345. <https://doi.org/10.1115/1.3119507>
- Ciorciari R, Kirik I, Niehuis R (2014) Effects of unsteady wakes on the secondary flows in the linear t106 turbine cascade. *J Turbomach* 136(9):091010. <https://doi.org/10.1115/1.4027374>
- Davide L, Simoni D, Ubaldi M, Zunino P, Bertini F (2017) Coherent structures formation during wake-boundary layer interaction on a lp turbine blade. *Flow, Turbulence and Combustion* 98(1):57–81. <https://doi.org/10.1007/s10494-016-9741-6>
- Denton JD (1993) Loss mechanisms in turbomachines. In: Turbo expo: power for land, sea, and air, vol. volume 2: combustion and fuels; oil and gas applications; cycle innovations; heat transfer; electric power; industrial and cogeneration; ceramics;

- structures and dynamics; controls, diagnostics and instrumentation; IGTI Scholar Award. <https://doi.org/10.1115/93-GT-435.V002T14A001>
- Dormand JR, Prince PJ (1980) A family of embedded Runge–Kutta formulae. *J Comput Appl Math* 6(1):19–26. [https://doi.org/10.1016/0771-050X\(80\)90013-3](https://doi.org/10.1016/0771-050X(80)90013-3)
- Duden A, Raab I, Fottner L (1999) Controlling the secondary flow in a turbine cascade by three-dimensional airfoil design and endwall contouring. *J Turbomach* 121(2):191–199. <https://doi.org/10.1115/1.2841301>
- Engber M, Fottner L (1996) The effect of incoming wakes on boundary layer transition of a highly loaded turbine cascade. *Loss Mech Unsteady Flows Turbomach AGARD-CP-571*
- Garth C, Wiebel A, Tricoche X, Joy K, Scheuermann G (2008) Lagrangian visualization of flow-embedded surface structures. *Comput Graph Forum* 27(3):1007–1014. <https://doi.org/10.1111/j.1467-8659.2008.01236.x>
- Günther T, Gross M, Theisel H (2017) Generic objective vortices for flow visualization. *ACM Trans Graph* 36(4):141–14111. <https://doi.org/10.1145/3072959.3073684>
- Hadwiger M, Mlejnek M, Theußl T, Rautek P (2019) Time-dependent flow seen through approximate observer killing fields. *IEEE Trans Vis Comput Graph* 25(1):1257–1266. <https://doi.org/10.1109/TVCG.2018.2864839>
- Haller G (2015) Lagrangian coherent structures. *Ann Rev Fluid Mech* 47(1):137–162. <https://doi.org/10.1146/annurev-fluid-010313-141322>
- Haller G, Yuan G (2000) Lagrangian coherent structures and mixing in two-dimensional turbulence. *Phys D Nonlinear Phenomena* 147(3–4):352–370. [https://doi.org/10.1016/S0167-2789\(00\)00142-1](https://doi.org/10.1016/S0167-2789(00)00142-1)
- Helman J, Hesselink L (1989) Representation and display of vector field topology in fluid flow data sets. *Computer* 22(8):27–36. <https://doi.org/10.1109/2.35197>
- Helman JL, Hesselink L (1991) Visualizing vector field topology in fluid flows. *IEEE Comput Graph Appl* 11(3):36–46. <https://doi.org/10.1109/38.79452>
- Hinterberger C, Fröhlich J, Rodi W (2008) 2D and 3D turbulent fluctuations in open channel flow with $Re \tau = 590$ studied by large eddy simulation. *Flow Turbulence Combust* 80(2):225–253. <https://doi.org/10.1007/s10494-007-9122-2>
- Hodson HP, Dawes WN (1998) On the interpretation of measured profile losses in unsteady wake-turbine blade interaction studies. *J Turbomach* 120(2):276–284. <https://doi.org/10.1115/1.2841403>
- Hodson HP, Howell RJ (2005) Bladerow interactions, transition, and high-lift aerofoils in low-pressure turbines. *Ann Rev Fluid Mech* 37(1):71–98. <https://doi.org/10.1146/annurev.fluid.37.061903.175511>
- Hussain AKMF, Reynolds WC (1970) The mechanics of an organized wave in turbulent shear flow. *J Fluid Mech* 41(2):241–258. <https://doi.org/10.1017/S0022112070000605>
- Kasten J, Petz C, Hotz I, Noack BR, Hege H-C (2009) Localized finite-time Lyapunov exponent for unsteady flow analysis. In: Magnor M, Rosenhahn B, Theisel H (eds) *Vision modeling and visualization*, vol 1, pp 265–274
- Koschichow D, Fröhlich J, Kirik I, Niehuis R (2014) DNS of the flow near the endwall in a linear low pressure turbine cascade with periodically passing wakes. In: *Turbo expo: power for land, sea, and air*, vol. volume 2D: turbomachinery. <https://doi.org/10.1115/GT2014-25071.V02DT44A001>
- Laramee R, Hauser H, Zhao L, Post F (2007) Topology-based flow visualization. *State Art*, pp 1–19. https://doi.org/10.1007/978-3-540-70823-0_1
- Mailach R, Vogeler K (2004) Aerodynamic blade row interactions in an axial compressor—part I: unsteady boundary layer development. *J Turbomach* 126(1):35–44. <https://doi.org/10.1115/1.1649741>
- Mayle RE (1991) The role of laminar-turbulent transition in gas turbine engines. In: *Turbo expo: power for land, sea, and air*, vol. volume 5: manufacturing materials and metallurgy; ceramics; structures and dynamics; controls, diagnostics and instrumentation; education; IGTI Scholar Award; General. <https://doi.org/10.1115/91-GT-261.V005T17A001>
- Michelassi V, Wissink JG, Fröhlich J, Rodi W (2003) Large-eddy simulation of flow around low-pressure turbine blade with incoming wakes. *AIAA J* 41(11):2143–2156. <https://doi.org/10.2514/2.6832>
- Michelassi V, Chen L-W, Pichler R, Sandberg RD (2015) Compressible direct numerical simulation of low-pressure turbines—part II: effect of inflow disturbances. *J Turbomach* 137(7). <https://doi.org/10.1115/1.4029126>
- Muthanna C (May 2002) The effects of free stream turbulence on the flow field through a compressor cascade. PhD thesis
- Nsonga B, Niemann M, Fröhlich J, Staib J, Gumhold S, Scheuermann G (2020) Detection and visualization of splat and antisplat events in turbulent flows. *IEEE Trans Vis Comput Graph* 26(11):3147–3162. <https://doi.org/10.1109/TVCG.2019.2920157>
- Nsonga B, Scheuermann G, Gumhold S, Ventosa-Molina J, Koschichow D, Fröhlich J (2020) Analysis of the near-wall flow in a turbine cascade by splat visualization. *IEEE Trans Vis Comput Graph* 26(1):719–728. <https://doi.org/10.1109/TVCG.2019.2934367>
- Perot B, Moin P (1995) Shear-free turbulent boundary layers. Part 1. Physical insights into near-wall turbulence. *J Fluid Mech* 295:199–227. <https://doi.org/10.1017/S0022112095001935>
- Perot B, Moin P (1995) Shear-free turbulent boundary layers. Part 2. New concepts for Reynolds stress transport equation modelling of inhomogeneous flows. *J Fluid Mech* 295:229–245. <https://doi.org/10.1017/S0022112095001947>
- Pope SB (2000) *Turbulent flows* by Stephen B. Pope. <https://doi.org/10.1017/CBO9780511840531>
- Praisner TJ, Allen-Bradley E, Grover EA, Knezevici DC, Sjolander SA (2007) Application of non-axisymmetric endwall contouring to conventional and high-lift turbine airfoils. In: *Turbo expo: power for land, sea, and air*, vol. volume 6: turbo expo, parts A and B, pp 653–661 (2007). <https://doi.org/10.1115/GT2007-27579>
- Reda K, Salvi AA, Gray J, Papka ME (2021) Color nameability predicts inference accuracy in spatial visualizations. *Comput Graph Forum* 40(3):49–60. <https://doi.org/10.1111/cgf.14288>
- Rojo IB, Günther T (2020) Vector field topology of time-dependent flows in a steady reference frame. *IEEE Trans Vis Comput Graph* 26(1):280–290. <https://doi.org/10.1109/TVCG.2019.2934375>
- Sarkar S (2008) Identification of flow structures on a LP turbine blade due to periodic passing wakes. *J Fluids Eng* 130(6). <https://doi.org/10.1115/1.2911682>
- Schlichting H, Gersten K (2017). *Boundary-layer theory*. <https://doi.org/10.1007/978-3-662-52919-5>

- Schreiber H-A, Steinert W, Küsters B (2000) Effects of Reynolds number and free-stream turbulence on boundary layer transition in a compressor cascade. *J Turbomach* 124(1):1. <https://doi.org/10.1115/1.1413471>
- Scillitoe AD, Tucker PG, Adami P (2017) Numerical investigation of three-dimensional separation in an axial flow compressor: the influence of freestream turbulence intensity and endwall boundary layer state. *J Turbomach* 139(2). <https://doi.org/10.1115/1.4034797>
- Spencer R, Przytarski P, Adami P, Grothe P, Wheeler A (2021) Importance of non-equilibrium modelling for compressors. In: Turbo expo: power for land, sea, and air, vol. volume 2c: turbomachinery—design methods and CFD modeling for turbomachinery; ducts, noise, and component interactions. <https://doi.org/10.1115/GT2021-58645>. V02CT34A003
- Stieger RD, Hodson HP (2003) The transition mechanism of highly-loaded LP turbine blades. In: Turbo expo: power for land, sea, and air, vol. volume 5: turbo expo 2003, parts A and B, pp 779–788. <https://doi.org/10.1115/GT2003-38304>
- Stieger R, Hollis D, Hodson H (2003) Unsteady surface pressures due to wake induced transition in a laminar separation bubble on a LP turbine cascade. In: Turbo expo: power for land, sea, and air, vol. volume 6: turbo expo 2003, parts A and B, pp 927–935. <https://doi.org/10.1115/GT2003-38303>
- Walker GJ (1993) The role of laminar-turbulent transition in gas turbine engines: a discussion. *J Turbomach* 115(2):207–216. <https://doi.org/10.1115/1.2929223>
- Wang P, Fröhlich J, Michelassi V, Rodi W (2007) Large eddy simulation of variable density turbulent axisymmetric jets. In: Friedrich R, Adams N, Eaton J, Humphrey J, Kasagi N, Leschziner M (eds.) Proceedings of 5th international symposium on turbulent shear flow phenomena, pp 1049–1054
- Weiss AP, Fottner L (1995) the influence of load distribution on secondary flow in straight turbine cascades. *J Turbomach* 117(1):133–141. <https://doi.org/10.1115/1.2835631>
- Wheeler APS, Dickens AMJ, Miller RJ (2017) The effect of non-equilibrium boundary layers on compressor performance. In: Turbo expo: power for land, sea, and air, vol. volume 2b: turbomachinery. <https://doi.org/10.1115/GT2017-64635>. V02BT41A040
- Wiebel A, Garth C, Scheuermann G (2007) Computation of localized flow for steady and unsteady vector fields and its applications. *IEEE Trans Vis Comput Graph* 13:641–51. <https://doi.org/10.1109/TVCG.2007.4293009>
- Wiebel A, Garth C, Scheuermann G (2005) Localized flow analysis of 2D and 3D vector fields. In: Brodlié KW, Duke DJ, Joy K (eds.) Data visualization 2005: proceedings of EuroVis 2005, pp 143–150. Eurographics Association, Aire-la-Ville, Switzerland. <https://doi.org/10.2312/VisSym/EuroVis05/143-150>. Eurographics Association
- Wissink JG (2003) DNS of separating, low Reynolds number flow in a turbine cascade with incoming wakes. *Int J Heat Fluid Flow* 24(4):626–635. [https://doi.org/10.1016/S0142-727X\(03\)00056-0](https://doi.org/10.1016/S0142-727X(03)00056-0)
- Wissink JG, Rodi W (2008) Numerical study of the near wake of a circular cylinder. *Int J Heat Fluid Flow* 29(4):1060–1070. <https://doi.org/10.1016/j.ijheatfluidflow.2008.04.001>
- Wissink JG, Zaki TA, Rodi W, Durbin PA (2014) The effect of wake turbulence intensity on transition in a compressor cascade. *Flow Turbulence Combust* 93(4):555–576. <https://doi.org/10.1007/s10494-014-9559-z>
- Wu X, Durbin PA (2001) Evidence of longitudinal vortices evolved from distorted wakes in a turbine passage. *J Fluid Mech* 446:199–228. <https://doi.org/10.1017/S0022112001005717>
- Zaki TA (2013) From streaks to spots and on to turbulence: Exploring the dynamics of boundary layer transition. *Flow Turbulence Combust* 91(3):451–473. <https://doi.org/10.1007/s10494-013-9502-8>
- Zaki TA, Wissink JG, Rodi W, Durbin PA (2010) Direct numerical simulations of transition in a compressor cascade: the influence of free-stream turbulence. *J Fluid Mech* 665:57–98. <https://doi.org/10.1017/S0022112010003873>